Aerospace Science and Technology 177 (2026) 112805

Contents lists available at ScienceDirect

Aerospace Science and Technology

journal homepage: www.elsevier.com/locate/aescte

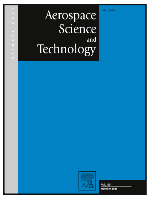

Fully-featured digital twins of in-service high-pressure turbine blades for high-fidelity CFD analyses

Pierluca Dessi [a,*], Mario Carta [a,b], Roberto Putzu [a], Shahrokh Shahpar [b], Tiziano Ghisu [a]

[a] *Department of Mechanical, Chemical and Materials Engineering, University of Cagliari, Via Marengo, 2, Cagliari, 09123, Italy*
[b] *Fluid Mechanics, Rolls-Royce plc, Derby, De24 8BJ, UK*

ARTICLE INFO

Communicated by Dr Mehdi Ghoreyshi

Keywords:
FFD Geometry morphing
High-pressure turbine
In-service deterioration
High-fidelity CFD

ABSTRACT

The high-pressure turbine blades of modern jet engines are inevitably subject to deformation and deterioration during their service life due to the extreme conditions under which they operate. Their hollow design with multiple internal cavities allows for effective internal and external cooling strategies, helping the component to withstand the increasingly high temperatures produced by modern combustors. Knowledge of the geometric variations experienced by these blades during service is crucial for designers to estimate the residual service life and aerothermal performance of the component. This important task has recently been achieved by running numerical flow simulations on the scanned, digitalized versions of the geometries.

For cost effectiveness, time savings, and practical reasons, the scanned geometries do not capture the complex internal channels of the component. This part of the geometry is vital to perform higher-fidelity assessments, such as conjugate heat transfer simulations, which model both internal and external flows.

This study proposes the first automatic methodology for reconstructing the internal geometry of a turbine blade scan by linking it to the external deformation field, paving the way for systematic generation of fully-featured digital twins of scanned in-service blade geometries. The internal deformation and reconstruction methodology is first presented in detail, then validated on a simplified test-case, and finally applied to a real high-pressure turbine blade scan from a modern jet engine. The resulting reconstructed geometry is used to assess the residual aerothermal performance of the scanned blade.

1. Introduction

A High-Pressure Turbine (HPT) blade is designed to operate under severe conditions, both in terms of thermo-physical loads (temperature, centrifugal, and pressure forces) and harsh environmental exposure (high-reacting flow from the combustor and ingested external particulates such as dust and debris). The extreme working conditions inevitably lead to in-service deformations, both on a large scale (untwisting) and on a smaller scale (thermal barrier coating loss and fouling). These deformations affect the exterior of the blade and its interior, modifying the internal cooling channels that run through the blade and provide an insulating layer of cooler air through a set of holes. The above modifications alter the aerothermal performance of the blade in two ways: on the one hand, aerodynamic performance is modified as a result of external deformations; on the other hand, the modified internals lead to different blade and film cooling behavior, and ultimately to different aerothermal performance.

Information obtained through residual performance assessment is useful for designers, as it gives insight into the blade deterioration and performance loss accumulated during the operational life, which can be leveraged to improve future designs. The effects of shape deformations on the residual performance of end-of-service blades have recently been evaluated through high-fidelity CFD (Computational Fluid Dynamics) simulations of the external flow, relying on simplified models, such as Crawford-type strip models [1], to surrogate the presence of cooling holes, thus neglecting the impact of internal geometry deformations on the cooling flow [2–7]. In [2], the authors performed automatic meshing and high-fidelity CFD of the external flow for 120 scanned blades, correlating shape variations with performance loss. In [3,4], the authors correlated shroud shape variations of 3D scanned end-of-service blades with heat transfer coefficient changes. In [5], a probabilistic CFD analysis on 500 3D-scanned new and service-exposed HPT blades was performed to study the correlation with geometric variability. In [6], the impact of various simulation fidelities was assessed using 25 scrapped

---

[*] Corresponding author.
E-mail address: pierluca.dessi@unica.it (P. Dessi).

https://doi.org/10.1016/j.ast.2026.112805
Received 6 March 2026; Received in revised form 17 May 2026; Accepted 2 June 2026
Available online 8 June 2026
1270-9638/

Nomenclature

$b_i^l(s)$	i-th Bernstein polynomial of degree l in the parametric coordinate s [-]
$\mathbf{d}_{CPi}$	Displacement vector of the i-th RBF control point [m]
$\mathbf{d}_{i,j,k}$	Displacement vector of the FFD control point (i, j, k) [m]
f_{Obj}	Objective function [-]
f_{tol}	Tolerance threshold for the norm of the Lagrangian gradient [-]
k	Number of knots per interpolator [-]
l_D	Distance loss term [m]
l_{D0}	Initial distance loss term for the design intent [m]
l_P	Penalty loss term [m]
l_{P0}	Initial penalty loss term for the design intent [m]
N_{sec}	Number of spanwise sections [-]
$T_{x,mid}$	Rigid body translation (chordwise, midspan) [m]
w_P	Weighting factor for penalty loss [-]
$\bar{\mathbf{x}}(s,t,u)$	Undeformed spatial position at (s,t,u) [m]
$\mathbf{x}(s,t,u)$	Deformed spatial position at (s,t,u) [m]
$\mathbf{x}_{CPi}$	Position of the i-th RBF control point [m]
BC	Boundary condition
CAD	Computer-aided design
CC	Curvilinear coordinate
CFD	Computational fluid dynamics
CFL	Courant-Friedrichs-Lewy
CHT	Conjugate heat transfer
CSF, CSD	Casing secondary inflows
CSV	Comma-separated value
DI	Design intent
EP	Engineering parameters
FEM	Finite-element method
FFD	Free-form deformation
HPT	High-pressure turbine
PS	Pressure-side
RANS	Reynolds-averaged Navier-Stokes
RBF	Radial basis functions
LE	Leading-edge
SLS	Structured light scanning
SLSQP	Sequential least-squares quadratic programming
SST	Shear stress transport
STL	Stereolithography
TBC	Thermal barrier coating
TE	Trailing-edge
TV	Thickness Variation
USH, DSH	Hub secondary inflows
α_i	Interpolation coefficient of the i-th control point [-]
$\boldsymbol{\delta}(s,t,u)$	Displacement vector at the dimensionless position (s,t,u) [m]
$\boldsymbol{\delta}(\mathbf{x})$	Displacement vector at the spatial position $\mathbf{x}$ [m]
$\phi(\cdot)$	Radial basis function kernel [-]

HPT blades. In [7], the authors employed CT scans to capture both the internal and the external geometry of turbine blades, and developed a mesh-morphing methodology that automatically maps boundary conditions from nominal CAD models to the as-manufactured components. They performed structural analyses of the scanned blades to assess their residual life.

The above studies necessitate the in-service blade's digital model, which is acquired through structured light scanning (SLS) techniques after engine overhaul. Currently, SLS techniques are the industrial standard for component scanning and are limited to digitalizing the outer shape of the blade [8,9]. As a result, the ability to perform higher-fidelity assessments, such as conjugate heat transfer (CHT) analyses, is prevented by the lack of internal geometry.

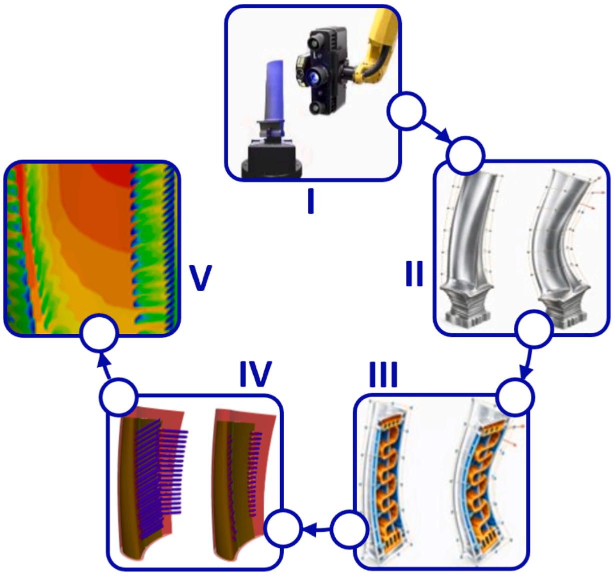

Fig. 1. Automatic workflow for fully featured conjugate simulation of scanned high-pressure turbine rotor blades. (I) Target structured-light scanning, (II) Nominal external shape distortion to match target, (III) Application of distortion matrix to internal, (IV) Full geometry merging and reconstruction (V) Meshing and Conjugate Heat Transfer simulation.

The reconstruction of external geometry alone is also an active field of research, with numerous studies recently conducted. Dammann et al. [10] developed a novel geometry reconstruction method applicable to compressor and turbine blades. Cheng et al. [11] developed a methodology to reconstruct drone propeller blade deflection based on real-time strain data, while Sterckx et al. [12] employed photogrammetry techniques to better predict the in-service leading-edge deterioration of wind turbine blades based on high-resolution images.

The objective of this work is to develop a fast and reliable technique to generate the internal cooling geometry of a 3D-scanned in-service blade, starting from the design-intent blade and the digital external model of the scanned blade. The methodology is graphically summarized in Fig. 1. The process starts from the acquisition of an in-service blade external surface through 3D scanning (phase I). Phase II is aimed at representing the variation in shape between the design intent (DI) blade and the in-service blade through a compact set of deformation variables, which are then used in phase III to produce deformed internals that match the exterior shape deformation experienced by the in-service blade. The in-service blade external surfaces and the new (deformed) internals are then merged in phase IV, The resulting geometry is then meshed and simulated with high-fidelity CFD to evaluate the residual performance of the in-service blade (phase V).

The methodology is based on FFD (Free-Form Deformation) [13] and RBF (Radial Basis Functions) [14] techniques.

While building on established techniques (such as FFD and RBF), mainly used in the context of shape optimization [15–18], this work proposes the first fast, automatic workflow enabling the reconstruction of a fully featured digital twin of an in-service HPT blade (including its internal channels for conjugate and film cooling) from a 3D scan of its external surface. Moreover, for the first time, a high-fidelity CHT analysis of an in-service blade is performed on the resulting fully-featured geometry. To the best of the authors' knowledge, no previous methodology in the literature enables such a complete reconstruction and analysis on a real degraded geometry. The aforementioned works [2–6] make use of inverse-mapping and deformation techniques for two main objectives: correlating performance variations with geometrical changes and/or obtaining a more precise location for cooling-hole source terms. The novelty of the proposed work lies in the use of deformation techniques to

Table 1
Simplified test-case DI geometric parameters at different spanwise sections.

Span [%]	10	50	90
Chord [mm]	185.7	188.4	192.6
Stagger Angle [deg]	27.4	29.5	33.4
Max Thickness/Chord [%]	33.9	28.2	25.0
Camber Angle [deg]	48.4	64.8	66.1
Aspect Ratio		1.3	

obtain a fully-featured in-service blade that enables higher-fidelity CFD and CHT analyses that would not be possible otherwise.

The present article is organized as follows. Section 2 introduces the two test cases defined in this work: the first one is a simplified turbine rotor geometry used to test and verify the approach extensively, the second one is a real turbine rotor geometry and its corresponding in-service 3D-scan, provided by Rolls-Royce plc. Section 3 details the methodology. Section 4 presents the results obtained on both the simplified test case and the real blade scan. Finally, in Section 5, conclusions are presented, highlighting the benefits and limitations of the current approach, as well as the impact of in-service deformations on the aerothermal performance of the HPT blade.

2. Description of the test cases

This section is dedicated to introducing the test-cases. The first one (described in Section 2.1) is a simplified turbine rotor geometry generated to test and verify the methodology. The second one (described in Section 2.2) is a real turbine rotor geometry with the corresponding SLS scan of an in-service specimen.

2.1. Simplified test-case

A simplified test-case was created to allow extensive testing of the methodology without restrictions on the presentation of the results due to confidentiality issues. First, a representative DI blade was generated using CAD tools, with cross-sections derived from the MT1 high-pressure turbine rotor design [19]. Table 1 summarizes the main geometrical parameters of at three different radial positions (10%, 50%, and 90% span). The blade features typical 3D characteristics, including spanwise chord variation and non-uniform distributions of both camber and stagger angles. These features ensure that the selected geometry serves as a robust and representative test-case for the proposed methodology.

The target blade was then obtained by applying a deformation, computed through a Finite-Element Method (FEM) displacement analysis, to the DI blade subjected to a hypothetical load. This procedure yields two versions of the target blade. The first is a watertight external surface, used as a replacement for an SLS scan to test the methodology. The second includes cooling holes and internal deformed geometry. Although the latter would not be available in a real-world scenario, it serves as a reference for comparing the reconstructed internal geometries.

Fig. 2 shows the test-case geometries, together with a comparison of the blade profiles at different heights. The internal geometry is presented through constant span cuts at 5 stations (0%, 25%, 50%, 75%, 100%) in Fig. 2(d), to highlight the differences. In Fig. 3, the distance field between the design intent and the target is shown as a contour plot on the surface of the target blade, reported in terms of chord percentage.

2.2. Real-world test-case

The second test-case used in the present work is represented by a rotor blade from a high-pressure turbine of a modern jet engine. The component presents a "firtree" type root which is meant to engage mechanically with the rotor disk, a blade section with a span of approximately 50 mm , and a "squealer-winglet" tip geometry. A schematic representing the main features of this kind of tip configuration is depicted in Fig. 4(a).

The blade design is hollow, with a series of internal cavities fed by a single inlet port in the root, and several cooling holes connecting the internal cavities with the exterior of the blade for film cooling purposes. The optical scanning technique performed using the GOM metrology suite [20] allows to capture the external shape of the component with an accuracy level of a tenth of a millimeter. The target blade was selected among a set of specimens from the same engine, as it presented all the main types of degradation commonly encountered in similar components. Compared with the DI geometry, the scanned blade displays a macroscopic twisting of the trailing edge (TE) towards the suction side below the winglet. Local TBC blistering is also present in the leading edge (LE) and pressure side (PS) regions, accompanied by a general increase in surface roughness. Erosion can be seen on the in-service blade squealer PS rim towards the trailing edge. The scanned blade presents a layer of thermal barrier coating (TBC) on its surface, which leads to an excess in thickness compared to the uncoated DI blade. This will be taken into account in the morphing procedure.

The single-row computational domain used for the present study is shown in the simplified scheme of Fig. 4(b). Various secondary inlets are present, including casing front inflow (CSF), casing downstream inflow (CSD), upstream hub (USH) and downstream hub (DSH) cavity inflows, as well as the front port film cooling (FC) inflow. The rotor geometry is fully featured and includes multiple internal cavities, tubes, and cooling holes. Two rotor geometries of such kind are considered for the present study, namely the design intent (DI) and the in-service one, the latter having been obtained through the morphing process detailed in the next section. The two rotor geometries share the same root component, which is the bottom part of the blade displaying the FC cooling port as visible in Fig. 4(b). The schematic section view displayed in Fig. 4(c) shows the distinction between the fluid (blue) and solid (grey) computational domains.

3. Methodology

Fig. 1 schematically illustrates the methodology developed to produce an automatic high-fidelity digital twin of the in-service blade. The procedure starts from the blade acquisition process that provides a watertight digital version of the external surface of the in-service blade (phase I in Fig. 1). Phase II aims to obtain a deformation field that is able to describe, with the necessary detail, the modifications that the in-service blade has experienced with respect to the DI shape. The same deformation field is then used in phase III to morph the blade internals, which in phase IV are joined to the digital external surface provided by phase I. Finally, in phase V, the fluid and solid domain enclosed by the internal and external surfaces are meshed, and a high-fidelity CFD assessment of the residual performance is completed. Detailed information on the methodologies introduced above is given in the following sections.

All codes are implemented in Python, using SciPy [21] and a modified version of PyGeM [22].

3.1. Blade acquisition (Phase I)

The blade acquisition process provides a digital model of the in-service blade under examination. The industrial standard for performing this process is through a 3D structured light scanner. The SLS technique is based on the use of a projector and a camera to scan an object. A structured light pattern is projected onto the scanned surface, while the camera captures the frames. The differences between the projected and scanned patterns are then used to reconstruct the object in 3D space

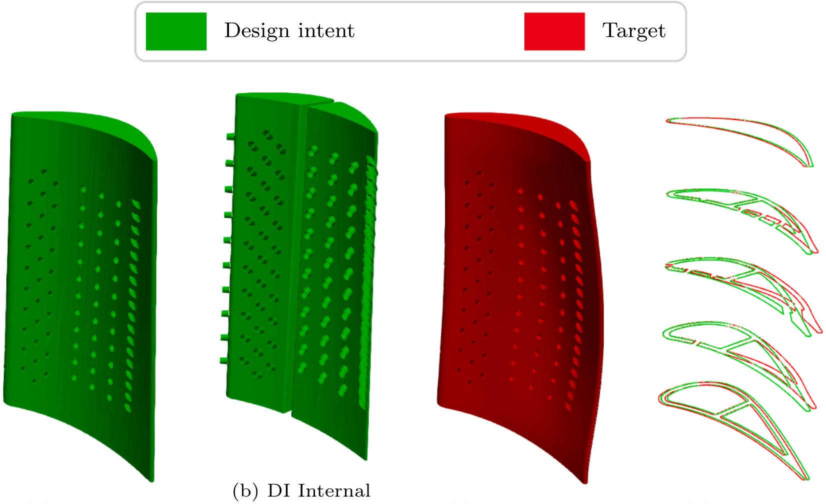

(a) DI blade
(b) DI Internal geometry
(c) Target blade
(d) Sections

Fig. 2. Simplified test case.

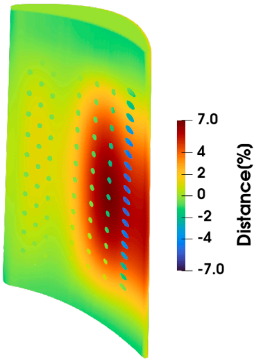

Fig. 3. Design-intent distance field - Simplified test case.

[23,24]. This process provides a watertight digital model that only represents the exterior surface of the blade, with an accuracy of 0.1 mm.

3.2. Geometrical deformation field (Phase II)

This step of the methodology aims to provide a deformation field that describes the variation in geometry occurring between the DI and the in-service blade, with the necessary detail. Deformative techniques for turbomachinery blades operate by modifying existing geometries (typically obtained through constructive methods, such as the ones based on CAD). A comprehensive overview of these techniques can be found in the literature [25,26]. Among the various approaches, Free-Form Deformation (FFD) and Radial Basis Functions (RBF) techniques are selected in this work due to their high flexibility, and are used as the basis to define the set of deformation parameters employed to morph the geometries. The latter will be described in detail in Sections 3.2.1 and 3.2.2.

Free-Form Deformation [13] is a technique that applies the deformation of a 3D lattice to the enclosed objects. The lattice is controlled by a set of control points whose displacements govern the resulting shape modification. The deformation of any entity within the lattice (points, curves, volumes) is calculated using the trivariate tensor product of Bernstein polynomials (Eq. (1)).

$$\boldsymbol{\delta}(s,t,u) = \sum_{i=0}^{l}\sum_{j=0}^{m}\sum_{k=0}^{n} b_i^l(s)\, b_j^m(t)\, b_k^n(u)\, \mathbf{d}_{i,j,k} \tag{1}$$

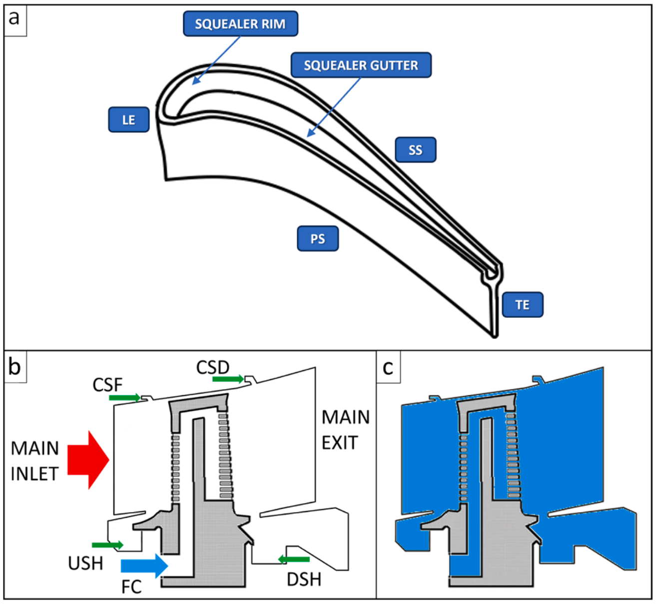

Fig. 4. Schematic view of the squealer-tip configuration considered in the present study. The geometry is characterized by an overhanging winglet and a rim going around the pressure and suction sides, forming a cavity called "gutter". The rim presents a discontinuity at the TE (a). Meridian view schematic of the domain used for CFD simulations (b), with a section of the rotor showing the internal cavities and cooling holes. The red arrow represents the main rotor inflow; the film cooling inlet is indicated in blue and secondary flow inlets in green. (c) Distinct regions for mesh generation, fluid region in blue and solid in grey. Meaning of the acronyms can be found in nomenclature - Schematic pictures distorted and not to scale. (For interpretation of the references to colour in this figure legend, the reader is referred to the web version of this article.)

where b_i^l, b_j^m and b_k^n denote Bernstein polynomials (the subscript indicates the basis index and the superscript the degree of the polynomial), while s, t and u are the normalized local coordinates $(0 \le s,t,u \le 1)$ of a generic point $\bar{\mathbf{x}}$ within the lattice. The term $\boldsymbol{d}_{i,j,k}$ represents the displacement of the (i,j,k) control point, and $\boldsymbol{\delta}(s,t,u)$ is the resulting displacement of the generic point at local coordinates s,t,u. The deformed position $\mathbf{x}(s,t,u)$ of the point is then computed by adding the displacement to the original coordinates.

In order to increase the flexibility of the method and its effectiveness in specific regions of the blade without having to escalate the number of control points, a B-spline interpolation is employed. The lattice itself remains uniformly spaced, whereas the deformation variables can be defined at arbitrary locations on B-spline surfaces corresponding to the envelope surfaces of the lattice. B-splines are preferred over linear interpolation due to their G^1 continuity, and over Bézier curves because they offer local support. Moreover, the movement of the internal FFD control points is obtained through bilinear interpolation from the displacement of the external control points. This reduces the dimensionality of the deformation problem without loss of flexibility, since no information on the internal deformation is available from the digitalized blade surface.

The initialization of the 3D lattice, which encloses the design intent blade, is done automatically, by evaluating its size and orientation. The lattice is aligned along a local reference frame (radial, chordwise and normal-to-chord directions), as this approach allows for an easier association between the lattice edges and key blade features (leading edge, trailing edge, suction side and pressure side), and an easier implementation of the Engineering Parameters approach described in Section 3.2.1. The alignment is performed automatically through an eigendecomposition of the points obtained from the DI blade surface.

The *Radial Basis Functions* [14] technique allows an existing object (points, curves, volumes) to be deformed by interpolating the displacements from a set of scattered control points, using, as the name implies, radial basis functions. Given a set of N control points $\{\mathbf{x}_{\mathbf{CP}_i}\}_{i=1}^{N}$ and their corresponding displacements $\{\mathbf{d}_i\}_{i=1}^{N}$, the displacement of an arbitrary point $\mathbf{x}$ is computed as reported in Eq. (2).

$$\delta(\mathbf{x}) = \sum_{i=1}^{N} \alpha_i \, \phi(\|\mathbf{x} - \mathbf{x}_{\mathbf{CP}_i}\|) + \mathbf{P}(\mathbf{x}) \tag{2}$$

In Eq. (2), $\phi(\cdot)$ denotes a radial basis function (e.g., multiquadric, Gaussian, thin-plate spline), $\|\cdot\|$ is the Euclidean distance, α_i are the interpolation coefficients, and $\mathbf{P}(\mathbf{x})$ is a low-degree polynomial added to improve accuracy and stability. The coefficients α_i and the ones of the polynomial $\mathbf{P}$ are computed by enforcing interpolation conditions at the control points. In this work, the thin-plate spline kernel is adopted for its smoothness and robustness.

3.2.1. *Engineering parameters (EP)*

Engineering parametrization incorporates the typical deformation modes of airfoils and turbomachinery blades, such as rigid body translations and rotations, recambering and chord adjustments. It is widely used in both performance optimization [27,28] and inverse-mapping tasks [29] as it typically results in a reduced and more interpretable design space.

A set of engineering deformations has been defined building on the FFD approach, including 6 EPs: rigid body translation, rotation, leading and trailing edge recambering and chord adjustments. A schematic of these deformations is shown in Fig. 5 and a complete description is given next:

- Rigid body translation: a uniform displacement is imposed on all control points of a section
- Rigid body rotation: a rotation matrix around the radial direction is applied pivoting around the section's centroid to compute the displacement of each control point
- Leading edge recambering: control points between the leading edge and a rotation center are rotated using a rotation matrix. The center of rotation is defined as a percentage of the chord and constrained to lie on the section's meanline [1]. The displacements of intermediate points are scaled (using a linear, parabolic, cubic, or intermediate power relationship) to yield zero displacement at points having the same chordwise coordinate as the center of rotation. Points aligned with or downstream of the center of rotation (i.e., toward the trailing edge) remain unaffected
- Trailing edge recambering: Same procedure as above, applied at the opposite end
- Leading edge chord length adjustment: control points between a starting point and the leading edge are translated chordwise. Displacements can be linear (zero at the start, prescribed at the leading edge) or piecewise linear (an intermediate point with specified position and displacement is added)
- Trailing edge chord length adjustments: Same procedure as above, applied at the opposite end

3.2.2. *Thickness variations (TV)*

The EP approach is not capable, by construction, to produce aerofoil thickness variations. To enable such variations, an RBF-based method is introduced.

The geometry is sliced at predefined span heights to extract blade sections. Each section is obtained by intersecting a constant-span plane with the STL edges, and the resulting points are subsampled to enforce a minimum spacing. These points serve as RBF control points.

To limit the number of design variables, control-point displacements are not assigned individually, but rather interpolated along the curvilinear coordinate via piecewise-linear functions defined by a set of knots. Pressure and suction sides of each section use separate interpolators. The number of deformation parameters is $N = (k-1) \cdot 2 \cdot N_{sec}$, where k is the number of knots per interpolator and N_{sec} the number of blade sections. The term $k-1$ reflects the constraint imposed to displacement values at LE and TE, identical for pressure and suction sides. The N parameters define the interpolators, which assign normal-direction displacements to all RBF control points. The RBF model finally applies the resulting deformation to the geometry, after a scaling performed to increase isotropy and interpolation quality.

Fig. 6 shows a schematic exemplifying the proposed approach for a generic two-dimensional airfoil section, using 18 RBF control points, $k = 5$ knots per interpolator.

3.2.3. *Definition of an optimal deformation*

The optimal values of the deformation parameters are selected through a minimization process based on the SLSQP algorithm [30]. The objective function is the sum of the unsigned L2 norms of the distances between the exterior of the morphed design intent blade and the target blade (the SLS scan).

As the SLSQP algorithm is gradient-based, a gradient evaluation is required at each iteration. Forward finite differences are employed due to their lower computational cost and satisfactory agreement with central finite differences, as shown in Fig. 7. The figure reports the derivative of the objective function with respect to a rigid body translation along the chordwise direction at the midspan section, for the simplified test case (described in Section 2.1), computed using forward and central finite differences with various step sizes. This behavior is consistently observed across all deformation variables.

The results presented in Fig. 7 (and the ones obtained for other deformation variables) are used to determine an appropriate step size. The optimal step size lies within a range presenting a stable value of computed gradient, thereby avoiding values that are too large - resulting in truncation errors - or too small - leading to rounding errors.

To further increase the fidelity of deformation and prevent unphysical displacements of the cooling holes, a penalty function is introduced. This requirement arises because the point-to-surface metric does not provide information about the position of the cooling holes, allowing unrealistic shifts (e.g., from leading to trailing edge). The procedure starts by identifying cooling holes in the design-intent external geometry, from non-manifold STL edges, and computing their centers. The

---

[1] The section's meanline is evaluated by computing, for each x-coordinate along the chord, the average of the n points with x-values closest to the chosen one. This enables an approximation of the meanline

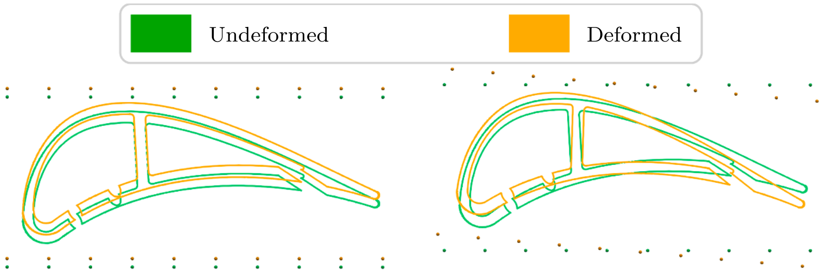

(a) Rigid body translation (b) Rigid body rotation

(c) LE recambering (d) TE recambering

(e) LE Chord Adj. (f) TE Chord Adj.

Fig. 5. Engineering deformations exemplification. The baseline profile and control points are shown in green, while the deformed ones are shown in orange. (For interpretation of the references to colour in this figure legend, the reader is referred to the web version of this article.)

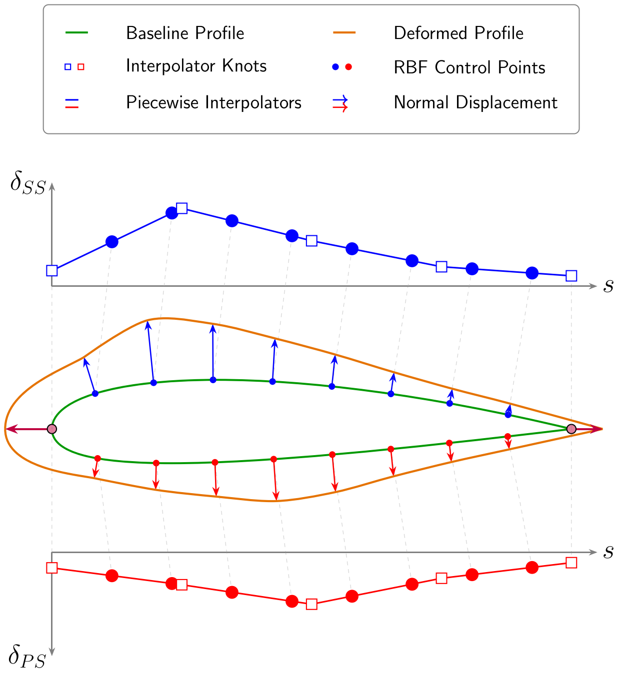

Fig. 6. Example of the TV approach with 18 RBF control points and 5 knots per interpolator.

corresponding centers in the target geometry are then loaded (e.g., from a CSV file), and one-to-one association is established.

During each deformation, the DI cooling holes are deformed accordingly. For each deformed cooling hole, a mean normal direction is computed via eigendecomposition. Then, using the normal unit vector and the centers of the deformed and target cooling holes, the distance orthogonal to the normal direction is calculated. The final penalty value is obtained by summing the constributions of all cooling holes.

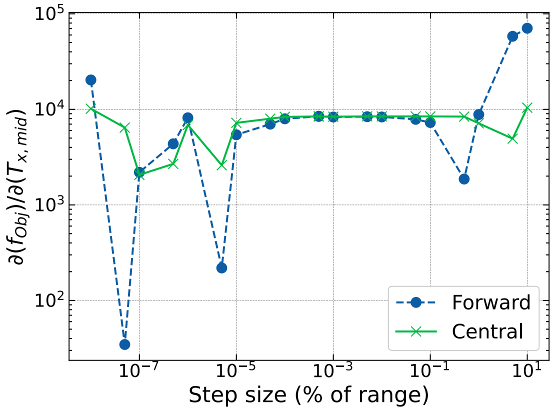

Fig. 7. Finite differences comparison.

Fig. 8 depicts a schematic exemplifying the penalty contribution calculation for a representative cooling hole, highlighting the three unit eigenvectors, the corresponding interpolating plane and the penalty value $d_{\perp}$.

The definition of an optimal deformation is needed in order to obtain a mapping between the design intent and the in-service geometry, enabling the internal features to be morphed consistently with the observed external deformations (Phase III). It is worth noting that this is the only objective of the external morphed geometry, as the final external surface used to build the final model is not the morphed geometry itself. Instead, the actual SLS scan is utilized during the merging phase (Phase IV), ensuring a perfect match between the digital twin's exterior and the scanned component.

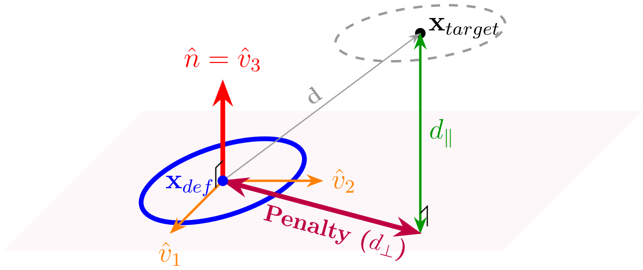

Fig. 8. Example of penalty computation showing the target and deformed cooling hole, the mean plane of the deformed cooling hole with its three unit eigenvectors, and the penalty distance $d_{\perp}$.

3.3. *Morphing of the internal geometry (Phase III)*

Once the optimal deformation is obtained, it is applied to the DI internal geometry, resulting in a morphed internal geometry. The result is an internal geometry consistent with the external scan of the in-service blade, up to the accuracy of the computed deformation field.

3.4. *Merging of internal and external geometries (Phase IV)*

In this phase, the deformed internal structure is merged to the original SLS scan. The latter does not include cooling holes, which must therefore be generated. This procedure is fully automated through a custom routine scripted in Blender [31], an open-source 3D software with built-in support for scripting and automation.

It comprises the following steps (illustrated in Fig. 9):

1. Isolation of the cooling passages. The cooling passages are selected from the deformed internal structure based on non-manifold boundary condition and clustered to reduce computational cost.
2. Extension of cooling passages. The cooling passages are extended in the normal direction to ensure intersection with the SLS scan.
3. Cooling holes generation. The extended passages are used to cut holes in the SLS scan, using boolean subtractions.
4. Passages trimming. The extended cooling passages are cut flush to the SLS scan using an automatically generated SLS scan negative volume.
5. Geometry merging. The trimmed passages are merged to the remaining part of the deformed internal structure, to the SLS and optionally to the design firtree, through vertex merging.

It is worth noting that geometric singularities, such as sharp edges and corners, are preserved throughout the process. Since the morphing framework (Phase II and III) applies a continuous displacement field to the datum geometry, any G^0 discontinuities present in the datum geometry are maintained. In all other regions, the transformation ensures that at least G^1 continuity is preserved. Furthermore, the automated merging routine utilizes boolean operations and selective vertex merging, ensuring that sharp features of the SLS scan are not modified.

3.5. *CFD Modelling methodology*

3.5.1. *CFD Meshing technique*

The fully-featured computational grids for both cases (DI, SLS) are generated with BOXER [32] using the same automated setup, by meshing directly on a "level-set" derived from the STL points. This enables various small-scale geometric features observable on the SLS surface, such as erosion and surface fouling, to be captured. In order to conduct CHT simulations, two domains are considered, namely the fluid one and the solid one, and a computational grid is generated for each domain. This is shown in Fig. 4(b), where the blue area represents the fluid domain and the gray area indicates the metal structure of the rotor (solid domain). 24 prismatic layers are generated by extrusion on all walls on the fluid domain side, with a first cell height set to achieve a y+ value below 1 on all surfaces. Local refinement is used to improve mesh resolution in critical areas such as the cooling tubes and internal turbulators. A mesh independence study is conducted to ensure grid-independent solutions with respect to the peak recovery temperature on the rotor surface. The results of the grid independence study for the DI case are reported in Table 2, as percentage variations with respect to the case with the highest mesh density (case "High"). Based on this study, the "Medium" mesh settings are selected.

Table 2
Mesh independence study on the DI case.

Case ID	Cells (Fluid)	Peak Temperature Delta
Low	224.2×10^6	2.4%
Medium	279.8×10^6	0.8%
High	325.3×10^6	-

A view of the fluid (blue) and solid (red) meshes with medium density setting is shown at the 50% span section view of Fig. 10(a), where local wall and wake refinements are visible. Part of the internal mesh structure is omitted from the representation for industrial confidentiality reasons. The prismatic layers around the walls, as well as the conformal mesh of the fluid-solid interface, are visible in the close-up view of Fig. 10(b), where the mesh is sectioned in correspondence with a cooling hole exit in the LE area. Mesh quality metrics pertaining to the two cases are quantified by Boxer, based on local aspect ratio, orthogonality and smoothness. It is found that, for the DI case, 96.95% of the mesh elements are classified with a quality level between 0.9 and 1 (maximum), compared to the 94.67% value achieved by the mesh on the SLS geometry. This indicates that the two meshes have remarkably similar quality levels.

3.5.2. *Numerical solving technique*

CFD simulations are run using the Rolls-Royce's proprietary density-based unstructured solver Hydra [33]. The 3D Reynolds-Averaged Navier-Stokes (RANS) equations are solved with an implicit scheme and a CFL of 20. The main inlet boundary condition (BC), indicated as "MAIN INLET" in Fig. 4, is represented by a two-dimensional field where total pressure, total temperature and inlet flow angles are specified. The boundary condition used for the internal cooling flow in the CHT setup is specified by imposing a two-dimensional field at the front root port entrance indicated by the blue arrow "FC" in Fig. 4, where total pressure,total temperature and inlet flow angles are specified. The secondary flow inlets indicated by green arrows in Fig. 4 are modeled by specifying the different mass flows, as well as temperatures and flow angles. Simulations are run on single-passage domains by enforcing periodic boundary conditions at the sides of the computational domain in the circumferential direction. The operating conditions simulated in this analysis are set to replicate an experimental thermal-paint test, used for validation purposes. For turbulence closure, the standard implementation of Menter's k-ω Shear Stress Transport (SST) turbulence model [34] is adopted. Convergence is achieved when the root-mean-square of the residuals for the momentum equations reaches 10^{-11}, corresponding to a 4-level drop in the residuals' order of magnitude, approximately after 6000 iterations. Before running the CHT simulations, an adiabatic-walls run is conducted on each case. The converged adiabatic-wall flowfields are used to initialize the solutions in the flow domains for the CHT simulations, whereas the temperature flow field in the solid domain is initialized using an uniform value. The coupling tool used to perform conjugate simulations is called JM76 and is part of the HYDRA system suite. Prior to each CHT simulation, coupling is established between the fluid and solid domains through the conformal contact interface between the two meshes. This relies on a search algorithm that, for each fluid boundary cell, finds the nearest solid cell across the interface. During the CHT simulations, a three-level geometric multi-grid explicit scheme is used to solve the heat conduction equation. Heat exchange

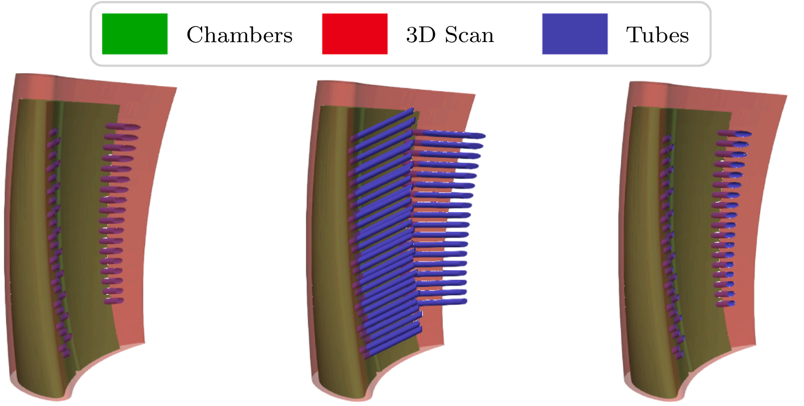

(a) Step 1 (b) Step 2 (c) Step 3, 4, and 5

Fig. 9. Exemplification of the merging procedure.

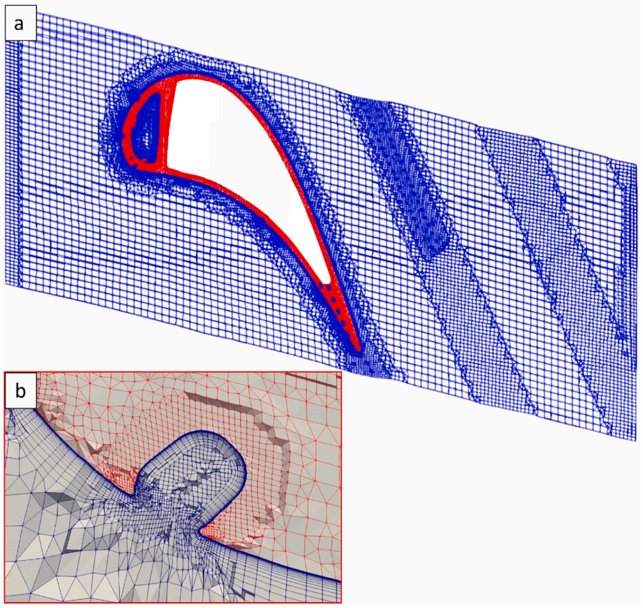

Fig. 10. Section view of the fluid (blue) and solid (red) meshes on the DI rotor case showing the local wall and wake refinements (a), and close-up view around one of the cooling holes showing the prismatic layers and the conformal interface between the meshes (b). Pictures distorted. Part of the internal cooling mesh omitted for industrial confidentiality reasons. (For interpretation of the references to colour in this figure legend, the reader is referred to the web version of this article.)

between the fluid/solid cell couples takes place periodically at intervals of 10 iterations for both domains.

3.6. Methodological assumptions and applicability

The key assumption of the proposed methodology is that the internal geometry deformations are driven by the modifications that the external geometry underwent during the component's service life. Consequently, the internal reconstruction mainly relies on the transfer of Engineering Parameters (EPs), which capture large-scale deformation modes such as untwisting.

The framework also enables localized features from the external surface to be captured and transferred to the internal geometry through the RBF-based thickness variation routine. In this context, the number of interpolator knots (k) acts as a geometric filter on the scale of deformations to be transferred. While a fine parametrization, characterized by a large number of knots, allows for the modeling of small-scale features such as TBC loss or blistering, its application is generally discouraged for real in-service components. Since such surface-level deteriorations typically do not physically propagate to the internal cooling passages, utilizing the parametrization density as a filter prevents the introduction of unphysical deformations into the reconstructed internal geometry.

This engineering choice is expected to be valid under typical service conditions, where the structural integrity of the blade is maintained and deformations are dominated by global stress fields. However, this assumption may fail in scenarios involving severe localized structural damage, where the correlation between external surface changes and internal geometry becomes decoupled. Furthermore, in cases of significant asymmetric surface-level deterioration, the optimization process might be influenced by these features. In such instances, the optimizer may optimize matching the regions with the highest geometric discrepancies (e.g., the pressure side), potentially leading to a deformation field that favors the alignment of one side of the blade while providing a less balanced representation of the global structural deformation.

4. Results

4.1. Simplified test-case

The simplified test case (introduced in Section 2.1) is used to test the capabilities of the morphing methodology presented in Section 3. The optimal morphing is performed with a combination of Engineering Parameters (EP; described in Section 4.1.1) and Thickness Variations (described in Section 4.1.2).

4.1.1. EP Morphing

For this approach, the full set of EPs introduced in Section 3.2.1 is used, namely (the number of variables per section used to model each relative EP is given in parentheses):

- Chordwise and perpendicular rigid body translations (2)
- Rigid body rotation around the radial direction (1)
- Leading and trailing edge recambering (6)
- Leading and trailing edge chord length adjustments (8)

The FFD lattice is set with a dimensionality of $20 \times 2 \times 20$ (chordwise, normal-to-chord, and spanwise directions). Active spanwise sections are located at 0%, 25%, 50%, 75%, and 100% of the span. The chordwise - normal-to-chord dimensionality is selected to accurately capture the engineering deformations. Only two control points are used in the normal-to-chord direction, as no large variations are expected along this direction, whereas the chordwise direction requires higher-order variations due to recambering. With 17 deformation parameters per section and 5

Table 3
Summary of adjustable parameter values for the simplified test-case (EP).

Configurable Parameter	Value
FFD dimensionality (chordwise, normal-to-chord, spanwise)	$20 \times 2 \times 20$
Active spanwise sections	0%, 25%, 50%, 75%, and 100%
Constrained spanwise sections	None
Engineering parameters	Full set 17 per section
w_P	0.15
f_{tol}	10^{-30}
Recambering law	Power relationship obtained by optimizer
Curvature weighting map	Mean curvature scaled between 1.0 and 4.0

active sections, this results in an optimization problem with $17 \times 5 = 85$ deformation parameters.

The cooling hole penalty is imposed using a weighting factor that gives 85% weight to the reduction in non-dimensionalized distance loss and 15% to the reduction in non-dimensionalized penalty:

$$f_{Obj} = w_P \frac{l_P}{l_{P0}} + (1 - w_P) \frac{l_D}{l_{D0}} \tag{3}$$

where l_{D0} and l_{P0} denote the distance loss and the penalty function, respectively, for the design intent. The weighting factor $w_P = .15$ was selected based on a sensitivity study reported later in this section. This value represents an optimal trade-off between external matching and cooling-hole positioning.

The cooling-hole centers of the target geometry are imported from a file generated from the target model that includes holes. A weighting map, dependent on blade curvature, is applied to the distances before their summation to enhance the reproduction of the leading and trailing edges[2] The weighting map is obtained by evaluating the mean curvature of the design-intent. The optimization stopping criterium is a maximum value for the norm of the Lagrangian gradient below the tolerance of $f_{tol} = 10^{-30}$ [21].

Table 3 provides a summary of the values selected for the adjustable parameters defined in the approach.

Fig. 11 reports the optimization history, non-dimensionalized by the DI value. The contribution of the distance loss alone is also shown in the same figure. The objective function achieved a reduction of 83.04%, with the penalty function reduced by 32.05% from its initial value, and the distance loss reduced by 92.04%. The process required 109 iterations, involving approximately 9,500 function evaluations (including the ones needed for gradient computation and line-search) and took approximately 2 hours on an MSI Katana GF66 laptop (Intel i7-12700H CPU, 16 GB RAM, using 16 cores for distance computation).

In Fig. 12, the final distance fields are reported in terms of chord percentage. In Fig. 12(a), the distance field is shown using the same range as in Fig. 3, to highlight the reduction achieved, while in Fig. 12(b), the same distance field is shown using a symmetric range scale defined by the maximum negative and positive distances.

Fig. 13 presents the morphed geometry at the midspan section, along with the target geometry (internal and external), highlighting the accuracy of the match. The EP approach captures the main deformations of the blade. The cooling holes are correctly aligned and the internal geometry (not used to drive the optimization as this information is not available in a real-world scenario) is also well represented. However, the internal partition wall is slightly rotated and some small bumps are not captured. The handling of these bumps is the goal of the following thickness variation procedure, described in Section 4.1.2.

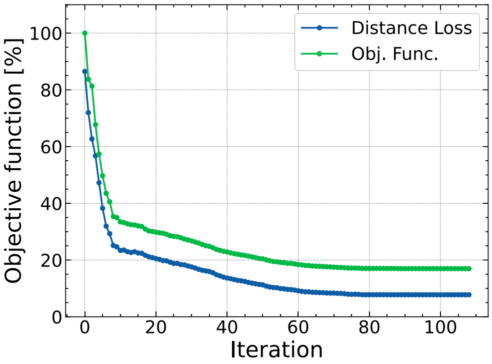

Fig. 11. EP optimization history - Simplified test case.

Effect of the penalty term

To demonstrate the effect and necessity of introducing the penalty function, a sensitivity study is performed varying the penalty weight. Fig. 14 shows the results obtained. On the horizontal axis, the value assigned to the weight factor w_P is reported. On the vertical axis, the penalty term and distance loss are shown, non-dimensionalized with the values calculated for the DI, l_{P0} and l_{D0}, respectively. Weight factor values larger than 50% are not investigated, as this would imply a higher importance given to the penalty function than to the distance loss.

As shown, when the penalty term is not included in the objective function formulation (i.e. $w_P = 0$) the maximum reduction in the distance loss is achieved, at the cost of an increase in the penalty term itself, indicating the cooling hole positioning has worsened even with respect to the datum internals. Increasing the weight factor leads to improved cooling hole positioning, as highlighted by the reduction in the penalty term, at the cost of slightly worse external matching, reflected by the higher distance loss. A plateau region can be identified for values of the weight factor between 5% and 20%. A weight factor of 15% is therefore selected, as larger values would lead to better cooling hole positioning but significantly worsen distance loss, and in this region the results appear to be robust with respect to the weight factor itself.

Fig. 15 presents a comparison between the target geometry and three geometries obtained with different penalty weights (0%, 15%, 40%) at the midspan section. The external surface matching is similar between the 0% and 15% cases. In contrast, the 40% case is not able to capture the blade exit angle correctly. The internal geometry fidelity increases with increasing weight penalty. However, the trailing edge misalignment strongly affects the last cooling hole row angle, which in this work is considered more important than the partition wall alignment.

4.1.2. *Thickness variation*

Starting from the geometry obtained through the EP morphing (Section 4.1.1), a thickness matching is applied through the RBF procedure introduced in Section 3.2.2. Five RBF sections (5%, 25%, 50%, 75%, 95%) are used, with a distance threshold that gives a total of 1,232 RBF control points. Their displacements are interpolated using 30 knots on pressure side and suction side for each section, leading to an optimization problem with $(30 - 1) \times 2 \times 5 = 290$ deformation parameters. Table 4 provides a summary of the values selected for the adjustable parameters defined in the approach.

Fig. 16 shows the optimization history, non-dimensionalized with the design-intent objective function loss (including the cooling-holes penalty to match the scale used in Fig. 11).

The objective function is reduced by 63.93% with respect to the initial value. The process required 32 iterations and approximately 9,400 objective function evaluations (including the ones for gradient computation and line-search) taking about 3 hours on the same laptop used for

---

[2] This affects the objective function reported later but not the distance fields.

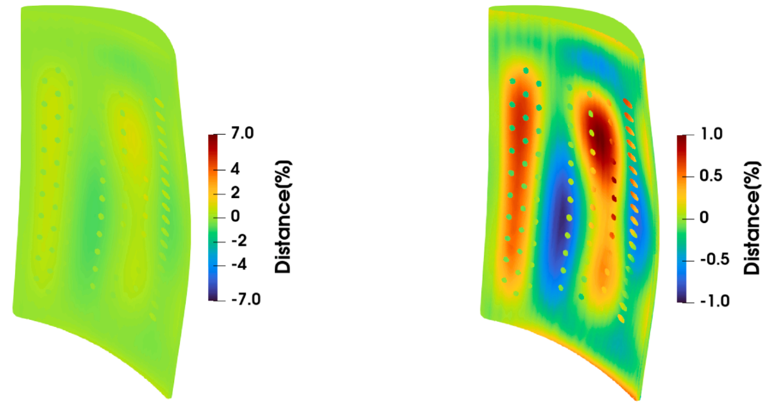

(a) Design-intent Range Scale (b) Optimal morphed geometry Range Scale

Fig. 12. EP Distance field - Simplified test case.

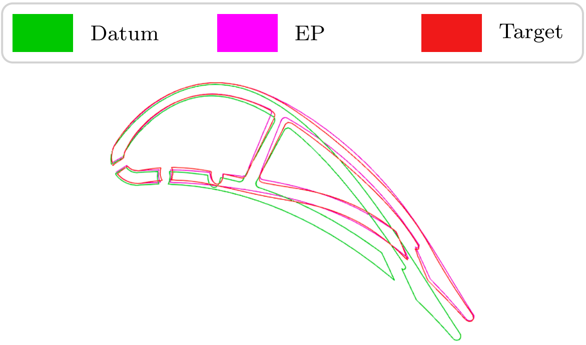

Fig. 13. EP Results (Midspan section) - Simplified test case.

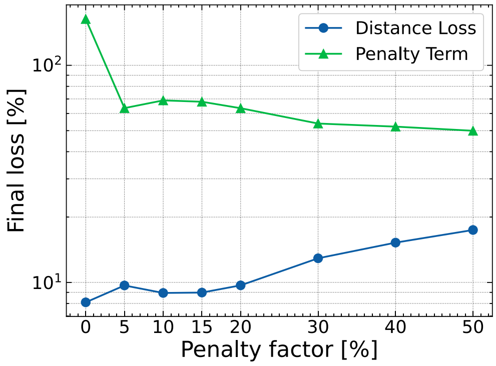

Fig. 14. Sensitivity analysis of the penalty factor.

Table 4
Summary of adjustable parameter values for the simplified test-case (TV).

Configurable Parameter	Value
Active spanwise sections	5%, 25%, 50%, 75%, and 95%
Constrained spanwise sections	None
Distance threshold	0.5% of the blade midspan chord
Interpolator knots k	30
f_{tol}	10^{-30}

the previous optimization, making the RBF deformation more computationally expensive.

In Fig. 17, the distance fields are shown. In Fig. 17(a), the distance field for the final geometry is shown using the same range as in Fig. 12(b), to highlight the differences, while in Fig. 17(b) it is presented with a symmetric range scale defined by the maximum negative and positive values. The external and internal geometries are also shown at the midspan section in Fig. 18, alongside the target geometry, to highlight the precision of the match.

The bumps not captured with the EP approach are correctly reproduced, providing a better representation of the deformed external and internal geometry, with the exception of the slight rotation of the partition wall separating the cooling chambers. However, the hub and tip sections appear slightly worse than without the TV application. This is due to the choice of the RBF sections, which are slightly offset from the hub and tip, necessitating extrapolation and resulting in some small inaccuracies.

4.2. Real-world test-case

For the real-world test case (introduced in Section 2.2), the morphing is performed only with the EPs, because the corresponding modes of deformation are the only ones that are assumed to be transferred to the internal blade geometry. Small scale deformations, such as TBC loss, blistering and fouling, do not cause deformations of the internal geometry and are deliberately not applied to this test case. It is worth noting that their effect is considered in the simulations thanks to the fact that the external digital model of the in-service blade, merged to the morphed internal, is directly used to construct the computational mesh, as explained in Section 3.4.

4.2.1. EP Morphing

The morphing based on the Engineering Parameters approach (introduced in Section 3.2.1) makes use of the full set of EPs as in the simplified test case (Section 4.1.1).

The FFD lattice has a dimensionality of $20 \times 2 \times 20$ (chordwise, normal-to-chord and spanwise directions). The sections are placed at 0%, 8%, 35%, 65%, 85.5% and 100% of the span, with sections at 0% and 100% constrained to have no displacement. For the hub section, this is required to re-attach the root before CFD meshing (the root was removed before the morphing procedure, ignoring its in-service deterioration). For the tip section, the constraint is used to exclude the complex winglet geometry from the objective function. After the optimization, the tip section is assigned the same displacements as the section just below (85.5% span). With 17 deformation parameters per section and 4 active sections, the optimization problem consists of 68 deformation parameters. Given the 4 active sections, it is considered appropriate to include every other cooling hole in the evaluation of the penalty function. Because these

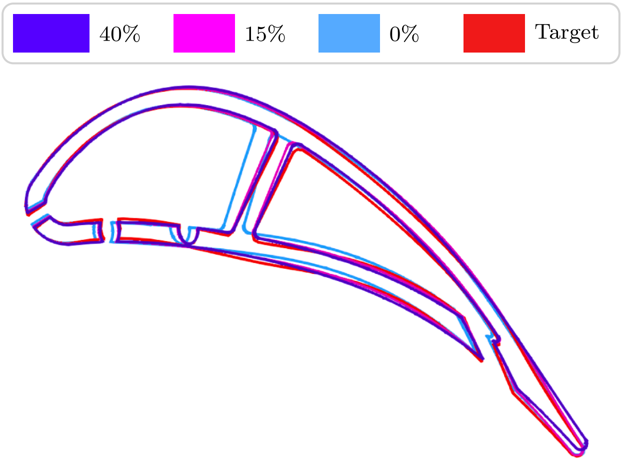

(a) Midspan section

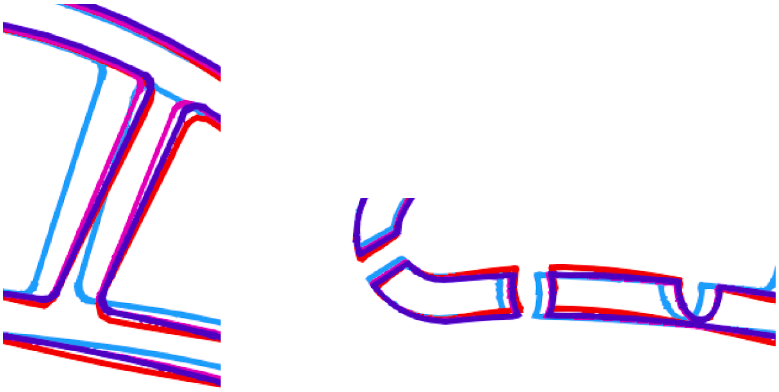

(b) Partition wall - zoom view (c) Cooling holes - zoom view

Fig. 15. Effect of the penalty function on the morphed geometry.

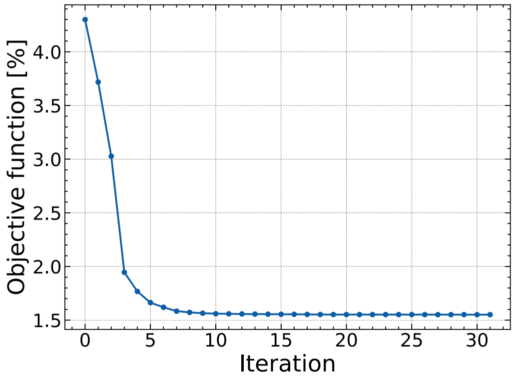

Fig. 16. TV optimization history - Simplified test case.

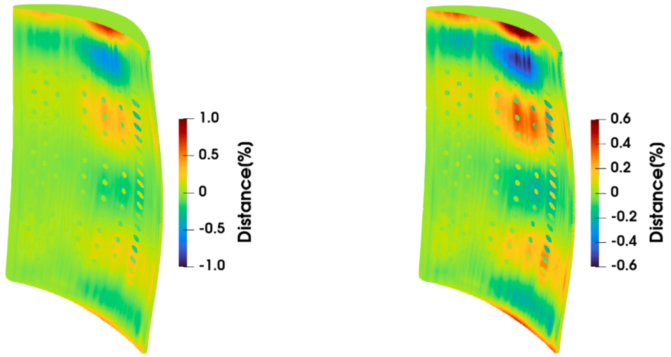

(a) EP Range Scale (b) TV Range Scale

Fig. 17. TV Distance field - Simplified test case.

data are unavailable from the SLS scan, the centers are manually identified on the SLS scan (thanks to the bumps at the holes locations). As explained in detail in Section 5.1 the uncertainty on the cooling hole positions is estimated to be of the order of 1/10 of its diameter, at least one order of magnitude lower than the misalignments in cooling hole position found with an unconstrained optimization. Therefore, the level of accuracy provided by the manual identification is considered sufficient.

Table 5 provides a summary of the values selected for the adjustable parameters.

The optimization history is shown in Fig. 19, non-dimensionalized with the DI value. The objective function is reduced by 16.44%. The optimization required 71 iterations, involving approximately $4,850$ function evaluations (including the ones for gradient computation and line-search). The distance loss is reduced by 24.32% from its initial value.

In Fig. 20, a comparison between the initial distance field (design intent vs. target SLS) and the final distance field (morphed geometry vs. target SLS) is shown, with a zoom on the suction side of the tip-section. In this region, the typical in-service deformation mode of high-pressure turbine blades is observed, namely, untwisting of the trailing-edge. This deformation mode is correctly captured by the methodology.

In Fig. 21, a comparison among the design intent, the target SLS and the morphed geometry is presented in the leading and trailing edge

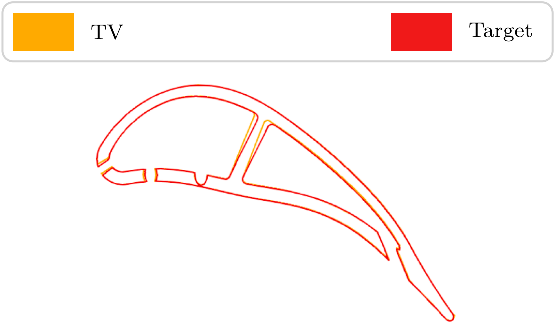

Fig. 18. TV Results (Midspan section) - Simplified test case.

Table 5
Summary of adjustable parameter values for the real-world test-case (EP).

Configurable Parameter	Value
FFD dimensionality (chordwise, normal-to-chord, spanwise)	$20 \times 2 \times 20$
Active spanwise sections	8%, 35%, 65%, and 85.5%
Constrained spanwise sections	0% and 100%
Engineering parameters	Full set 17 per section
w_P	0.15
f_{tol}	10^{-30}
Recambering law	Power relationship obtained by optimizer
Curvature weighting map	None

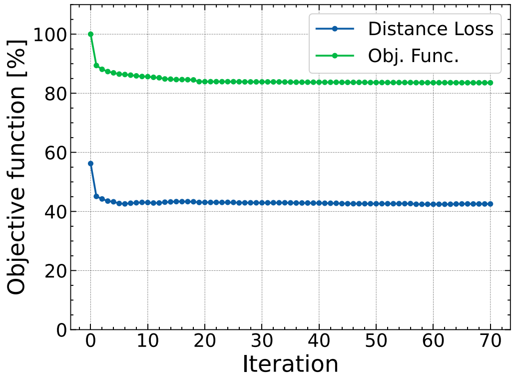

Fig. 19. EP optimization history - Real test case.

regions, through a section taken just below the winglet. The morphed geometry more closely reproduces the leading-edge chord adjustment and the trailing-edge recambering. This improvement comes at the cost of a slightly larger distance on the trailing-edge pressure side.

The reduction in distance loss obtained in the real-world test case is considerably lower than the one obtained for the simplified test case (Section 4.1.1). This is attributed to two main factors:

- The scanned geometry contains surface irregularities due to fouling and TBC loss, which are intentionally not captured by the parametrization used for the deformation.
- The scanned geometry is a coated blade, whereas the DI is not. This introduces an extra thickness that is intentionally not captured by the parametrization.

Both factors do not impact the fidelity of the external representation, as the final blade geometry used to perform the CFD simulation is obtained by merging the morphed internals with the digitalized SLS scan, as explained in Section 3.4. At the same time, this approach allows deformation modes not expected to be transferred on the internal blade geometry, such as TBC loss, blistering, and fouling, to be filtered out.

4.2.2. Conjugate heat transfer simulations

This section presents the results obtained through CHT simulations on the DI and on the in-service blades. The surface metal temperatures predicted for the DI are first validated against experimental data obtained through a thermal paint test. The test consists in coating a number of high-pressure turbine rotor blades with thermally-sensitive paints. The paints are characterized by an "activation" temperature range that, when reached, causes the paint to undergo a change in color. The engine is then re-assembled and subsequently powered up to conditions similar to its maximum take-off operating point, inside a testbed facility. After the test, the painted high-pressure turbine blades are extracted from the engine and the local coloration of the blades is traced back to the temperatures reached by the surface, through appropriate calibration coefficients followed by weighted averaging. It is worth noting that, given that thermal paints are activated in discrete ranges of temperatures, the experimental data have a resolution lower than other experimental and numerical approaches. This leads to the segmented appearance of the experimental temperature band in Fig. 22.

The results of the validation study are presented in Fig. 22 for a section at 50% span, which corresponds to the blade height where peak temperatures are reached for this case. The plot shows the external metal temperatures along the blade section as a function of its curvilinear coordinate (CC) comparing the values obtained through the experimental test (red band) against the CHT prediction (black curve). Similar agreement is observed at other sections taken at different span heights, which are not reported here for brevity. Positive values of CC refer to the pressure side of the blade, negative values refer to the suction side. The peak temperature area is located at 50% span for CC values between 35 and 55, pointing to the mid-chord pressure side area. As visible in Fig. 22, the conjugate model shows a good level of agreement with the experimental data, although some moderate under-prediction of the peak temperature values is observed. The tendency of the present steady-state CHT model towards a slight under-prediction of peak temperatures has previously been observed for similar high-pressure turbine cases [3,35].

A comparison between the CHT temperature predictions obtained for the DI and the in-service blade is reported in Fig. 23, where the temperature delta between the two is plotted against the blade curvilinear coordinate for the same midspan section. The temperature delta is mostly positive, indicating an overall hotter surface for the SLS case with respect to the design intent. There are localized areas where the temperature reached in the SLS case is lower than the one reached by the design intent case, and this is indicated by the negative spikes shown in Fig. 23, corresponding to curvilinear coordinate values of approximately 15 and 25. The CHT-predicted metal temperatures on the surface of the in-service case in the leading edge area ($-10 < CC < 10$) reach considerably higher values than the corresponding ones for the DI case. However, a temperature increase in this region is relatively less critical than the albeit more moderately higher temperature reached by the in-service case in the mid-span pressure-side area ($35 < CC < 55$), because this is the part of the surface where the overall peak temperatures are reached. These temperature increases are due to a number of factors, notably the partial obstruction of several cooling holes as a result of fouling and the higher heat exchange as a result of the increased surface roughness characterizing the scanned blade.

The increase in temperature for the in-service blade is visible in Fig. 24, which shows static temperature contours in the mid-span pressure side region for the DI (a) and in-service (b) blades, compared with a close-up picture of the same area (c) taken on a real in-service blade of the same model. As shown in the figure, the in-service blade is experiencing approximately 50K higher temperatures in the peak temperature region. It is interesting to note that high levels of erosion and loss of TBC

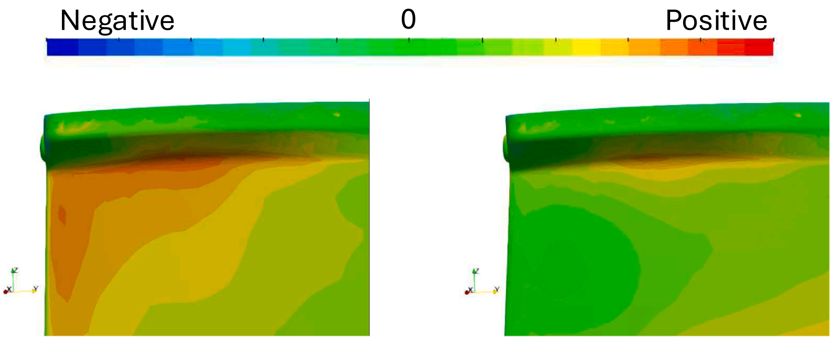

(a) Initial DF (b) Final DF

Fig. 20. Distance fields comparison at the tip-section suction side - Real test case.

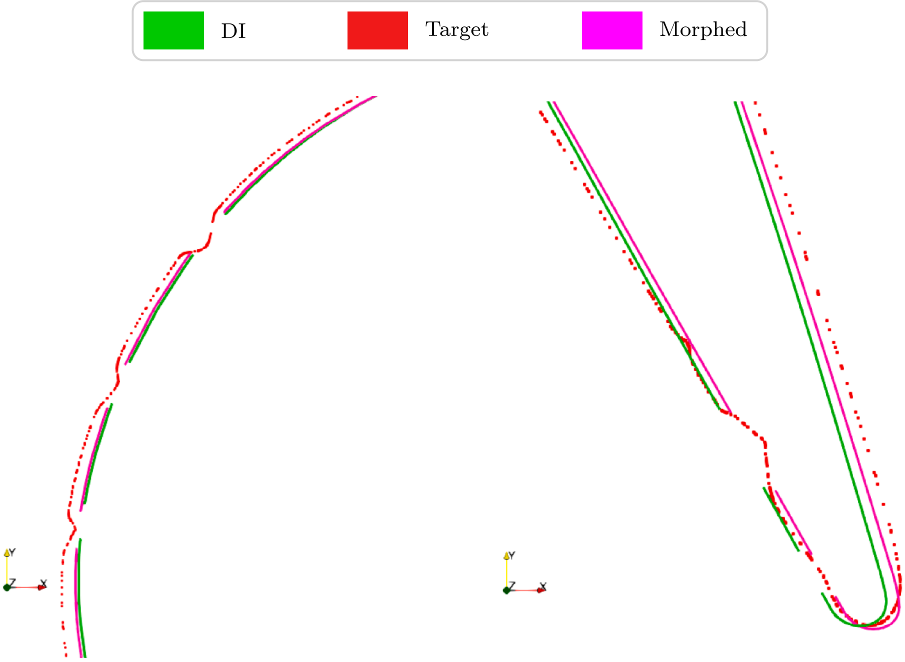

(a) LE (b) TE

Fig. 21. Leading and trailing edge comparison between design-intent (green), the target (red), and the morphed geometries (purple) at the section just below the winglet, for the real test case. (For interpretation of the references to colour in this figure legend, the reader is referred to the web version of this article.)

(the black discoloration on the right side of Fig. 24(c) as opposed to the white ceramic coating on the left) can be observed in this region for the in-service specimen. It is important to note that, in the DI geometry, a "fan-shaped" bevel is present at the outer edge of each cooling hole (see Fig. 24(a)). The TBC spraying process itself and in-service fouling can reduce the bevel's radius and produce a partial blocking effect on the cooling holes [36,37]. In some specimens, such as the one considered for the present study, the outer bevel of most of the cooling holes is completely absent, as visible in the example portrayed in Fig. 24(c). The current morphing process replicates this phenomenon by intersecting the cooling tubes directly with the SLS surface, producing cooling holes with unbeveled outer edges. As a result of this, the trajectory of the film cooling flow exiting the holes appears to be noticeably more lifted from the external surface. Fig. 25 shows a visualization of the streamlines for the coolant exiting the central cooling hole of Fig. 24, for the DI (a) and in-service (b) cases. In Fig. 25, the black curves indicate sections of the external surface of the blades aligned with the coolant flows exiting the cooling holes. The coolant in the in-service case with the unbeveled cooling hole edge experiences significant lift-off from the surface due to the sharper edge. The bump observable immediately downstream of the cooling holes in Fig. 25(b), likely due to fouling buildup, further exacerbates this phenomenon. The increased lift-off has a detrimental effect on film cooling effectiveness downstream of the cooling holes. As found by the present CFD analysis, this is also associated with a significant overall reduction in the total cooling mass flow of approximately 6.5% in the in-service case compared to the DI case, both obtained with the same pressure-based cooling inflow boundary condition.

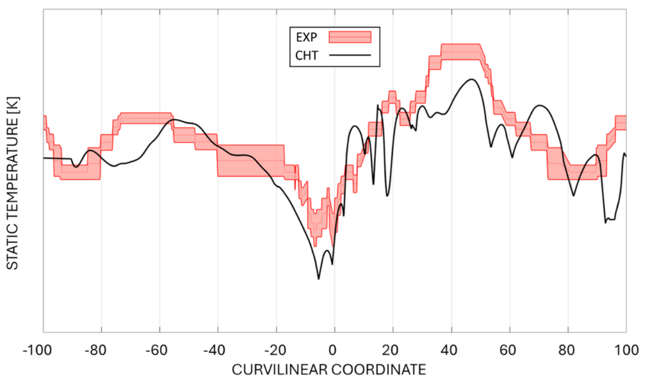

Fig. 22. Comparison between the CHT prediction for the DI case (black curve) and thermal paint experimental data (red curve) at a midspan section of the blade's external surface, in terms of static metal temperatures along the section's curvilinear coordinate (CC); values on the vertical axis removed for industrial confidentiality. The experimental data is presented with its variability band (plus or minus one standard deviation). (For interpretation of the references to colour in this figure legend, the reader is referred to the web version of this article.)

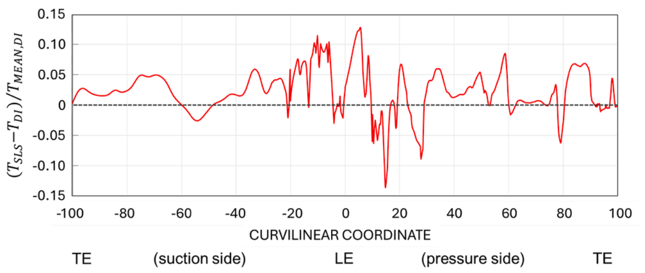

Fig. 23. Comparison between the CHT predictions for the DI and morphed SLS cases at a midspan section of the blade's external surface, in terms of static metal temperature difference $\Delta T = T_{SLS} - T_{DI}$ non-dimensionalized by the mean DI temperature $T_{MEAN,DI}$ along the section's curvilinear coordinate.

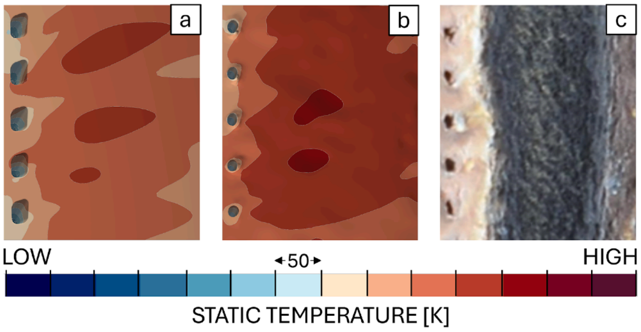

Fig. 24. Temperature contours predicted by CHT simulations on the DI (a) and in-service (b) cases in the peak temperature area located at the mid-span mid-chord position. Part of a cooling hole row can be seen in the left side of the pictures. Contours are compared with a close-up picture of the same area taken on a in-service blade of the same model (c). The white color indicates the presence of TBC, whereas the blackened area indicates erosion of the thermal coating. The absence of bevels on the outer edges of the cooling holes is also visible.

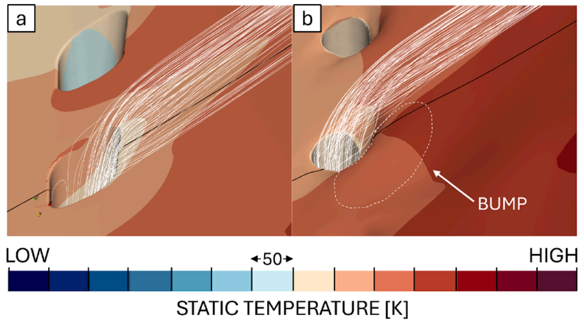

Fig. 25. Streamlines of the coolant particles exiting the central cooling hole of Fig. 24 for the DI (a) and in-service (b) cases. The surface of the blades is coloured by contours of static temperature. The black curves represent sections of the blades' external surfaces aligned with the direction of the cooling flows to indicate the amount of lift-off experienced by the cooling flow. The presence of a bump caused by fouling buildup downstream of the cooling hole is highlighted.

5. Discussion and conclusions

5.1. Limitations

Beyond the physical assumptions discussed in Section 3.6, some practical limitations remain.

First, the manual identification of cooling hole centers on the target SLS scan introduces a potential source of uncertainty. To quantify this effect, the identification process was repeated five times. The resulting maximum uncertainty, expressed as a standard deviation, was found to be of the order of $1/10$ of the cooling-hole diameter. By comparison, when no penalty constraint is applied to the cooling-hole positions ($w_P = 0$), the displacement error can reach the same order of magnitude as the hole diameter itself. Since the uncertainty resulting from manual selection is an order of magnitude smaller than the potential unconstrained morphing error, its impact on the reconstruction is considered negligible.

Second, the lack of non-destructive internal scan data (e.g., CT scans) for the real-world test-case prevents a direct geometric validation of the reconstructed internal cooling passages.

Third, the overall wall-clock time required by the process is still not appropriate for large-scale industrial applications. To provide a clearer overview of the process efficiency, the indicative time requirements for each phase are summarized below:

- Phase I: The SLS acquisition process typically requires approximately 30–45 minutes, factoring in the scanning, digitalization and inspection report phases.
- Phase II: Evaluating the optimal deformation field takes approximately three hours for the Engineering Parameters approach alone, increasing to roughly seven hours when Thickness Variations are included. In this phase, the manual identification of cooling-hole centers takes approximately 15 minutes.
- Phase III: The morphing of the internal geometry is highly efficient, requiring only one to three minutes.
- Phase IV: The automated merging of internal and external geometries typically takes between 30 minutes and one hour.
- Phase V: Preparation and execution of the CHT simulations, including preprocessing, meshing and solving requires approximately a week, using Windows-based CAD systems to perform the initial geometry treatment operations, and linux-based HPC parallel computing on around 240 processors for both the meshing and solving routines.

Consequently, the cumulative time cost suggests that while the methodology is robust for high-fidelity digital twin generation, it is not yet optimized for high-throughput, rapid inspection cycles in an industrial production environment.

Finally, although the proposed methodology enables the isolation of performance impacts stemming from external surface modifications (such as fouling and TBC loss) and internal geometry deformations, this decoupling was not explored in the current study due to the significant computational effort required for multiple high-fidelity CHT simulations.

In principle, this type of decoupling could be achieved by evaluating the performance across the following four geometric configurations:

1. Design Intent: establishes the baseline performance of the ideal component.
2. Fully-featured SLS scan: captures the combined effect of all in-service degradations and distortions.
3. Morphed external + Morphed internal: By joining the morphed internal passages with a reconstructed "clean" morphed external surface, the contribution of localized surface modifications is excluded.
4. Corrected SLS scan + Internal design intent: Applying a deformation field to the SLS scan to match the external design-intent profile, while retaining the internal design intent geometry, isolates the contribution of localized surface features from large-scale distorsions such as restaggering.

However, given the extensive computational resources required for each numerical run, such a parametric investigation remains outside the present scope and is reserved for future work.

5.2. Conclusions

This work presents a novel morphing methodology for reconstructing the internal geometry of an in-service high-pressure turbine blade starting from external 3D scans, addressing a key limitation in current literature. The approach enables high-fidelity aerothermal performance assessment of in-service film-cooled turbine blades.

The proposed approach was first validated on a simplified test case, showing good accuracy and a reasonable computational cost, making it suitable for industrial applications. It was then applied to a real-world engine blade, enabling high-fidelity CFD and CHT analyses on an in-service geometry from a high-pressure turbine rotor blade of a modern commercial jet engine.

Steady-state conjugate heat transfer simulations were performed on the design intent blade and on the in-service geometry obtained through the morphing procedure, modeling the internal cooling flow, as well as the main passage and secondary cavity flows. This was done to highlight the effects of in-service deterioration on the external metal temperatures.

The conjugate heat transfer results on the design intent geometry showed good agreement with the experimental thermal paint test. Compared to the design geometry, the in-service blade exhibited significantly higher temperatures in the leading edge area and higher peak temperatures in the mid-span pressure side area. For the same total coolant input pressure, the coolant mass flow generated by the SLS case was found to be 6.5% lower. This effect was attributed to the partial obstruction of the cooling holes by irregularities and fouling on the blade surface, resulting in a partial blockage effect and lower film cooling effectiveness.

Future work will address a broader validation of the internal reconstruction, including different blade families and cooling patterns, as well as variability and uncertainty assessment on both the reconstructed geometry and on the residual performance. Furthermore, future efforts will aim to systematically decouple the performance impacts of external surface degradations (e.g., fouling and TBC loss) from those induced by internal structural deformations.

CRediT authorship contribution statement

Pierluca Dessi: Writing – original draft, Visualization, Validation, Software, Investigation, Formal analysis, Data curation, Conceptualization; **Mario Carta:** Writing – review & editing, Visualization, Validation, Methodology, Investigation; **Roberto Putzu:** Software, Conceptualization; **Shahrokh Shahpar:** Writing – review & editing, Supervision, Resources, Conceptualization; **Tiziano Ghisu:** Writing – review & editing, Supervision, Resources, Project administration, Methodology, Conceptualization.

Data availability

The data that has been used is confidential.

Declaration of competing interest

The authors declare the following financial interests/personal relationships which may be considered as potential competing interests: This work has been conducted within the framework of the NEXTAIR project. The NEXTAIR project has received funding from the European Union's Horizon Europe research and innovation programme under grant agreement No. 101056732. The views and opinions expressed in this work are those of the authors only and do not necessarily reflect those of the European Union or REA. Neither the European Union nor the REA can be held responsible for them.

Acknowledgments

Development and applications of digital twins of engine components were carried out as part of the NEXTAIR project, funded by the European Union under Grant Agreement No. 101056732. The views and opinions expressed in this work are those of the authors only and do not necessarily reflect those of the European Union or REA. Neither the European Union nor the REA can be held responsible for them. The authors would like to thank Rolls-Royce plc for their support and permission to publish this work.

References

[1] M.E. Crawford, W.M. Kays, R.J. Moffat, Full-Coverage Film Cooling on Flat, Isothermal Surfaces: Data and Predictions, Technical Report NASA-CR-3219, NASA, 1980.
[2] M. Carta, T. Ghisu, S. Shahpar, High-fidelity computational fluid dynamics analysis of in-serviced shrouded high-pressure turbine rotor blades, J. Turbomach. 144 (12) (2022) 121001. https://doi.org/10.1115/1.4055267
[3] M. Carta, T. Ghisu, S. Shahpar, Multi-fidelity heat transfer analysis of shrouded high-pressure turbine rotor blades, in: ASME Turbo Expo 2023: Turbomachinery Technical Conference and Exposition, American Society of Mechanical Engineers, 2023, pp. V13BT30A038. https://doi.org/10.1115/GT2023-103789
[4] M. Carta, T. Ghisu, S. Shahpar, Heat transfer analysis of damaged shrouded high-pressure turbine rotor blades, Int. J. Turbomach. Propuls. Power 8 (3) (2023) 24. https://doi.org/10.3390/ijtpp8030024
[5] J. Scharfenstein, K. Heinze, M. Voigt, K. Vogeler, M. Meyer, Probabilistic CFD analysis of high pressure turbine blades considering real geometric effects, in: ASME Turbo Expo 2013: Turbomachinery Technical Conference and Exposition, American Society of Mechanical Engineers, 2013, pp. V06BT43A005. https://doi.org/10.1115/GT2013-94161
[6] W.Y. Lee, W.N. Dawes, J.D. Coull, The required aerodynamic simulation fidelity to usefully support a gas turbine digital twin for manufacturing, J. Glob. Power Propuls. Soc. 5 (2021) 15–27. https://doi.org/10.33737/jgpps/132007
[7] A. Ferhat, N. Anello, C. Remacha, H. Proudhon, D. Ryckelynck, Automated real turbine-blade lifetime prediction: from X-ray data to auto registration of boundary conditions in partial differential-equation models, Results Eng. (2026) 110721. https://doi.org/10.1016/j.rineng.2026.110721
[8] M. Javaid, A. Haleem, S. Pratap,S. Ravi, R. Suman, Industrial perspectives of 3D scanning: features, roles and it's analytical applications, Sens. Int. 2 (2021) 100114. https://doi.org/10.1016/j.sintl.2021.100114
[9] B. Gapinski, M. Wieczorowski, L. Marciniak-Podsadna, B. Dybala, G. Ziolkowski, Comparison of different method of measurement geometry using CMM, optical scanner and computed tomography 3D, Procedia Eng. 69 (2014) 255–262. https://doi.org/10.1016/j.proeng.2014.02.230
[10] M. Dammann, B. Schulten, J. Goeing, M. Steiner, M. Koster, J. Friedrichs, J.R. Seume, L. Wein, Maintenance of Jet Engines: Robust Parametrisation and Reconstruction of Compressor and Turbine Blades, American Society of Mechanical Engineers Digital Collection, 2025. https://doi.org/10.1115/GT2025-151573

[11] L. Cheng, H. Sheng, H. Feng, B. Hu, Accurate online reconstruction algorithm for UAV propeller blade deformation by FBG sensing, Aerosp. Sci. Technol. 176 (2026) 112105. https://doi.org/10.1016/j.ast.2026.112105

[12] J. Sterckx, M. Vlaminck, K. De Bauw, H. Luong, Accurate and robust 3D reconstruction of wind turbine blade leading edges from high-resolution images, Autom. Constr. 175 (2025) 106153. https://doi.org/10.1016/j.autcon.2025.106153

[13] T.W. Sederberg, S.R. Parry, Free-form deformation of solid geometric models, ACM SIGGR. Comput. Graph. 20 (4) (1986) 151-160. https://doi.org/10.1145/15886.15903

[14] A. de Boer, M.S. van der Schoot, H. Bijl, Mesh deformation based on radial basis function interpolation, Comput. Struct. 85 (11) (2007) 784–795. https://doi.org/10.1016/j.compstruc.2007.01.013

[15] X. Tang, J. Luo, F. Liu, Adjoint aerodynamic optimization of a transonic fan rotor blade with a localized two-level mesh deformation method, Aerosp. Sci. Technol. 72 (2018) 267–277. https://doi.org/10.1016/j.ast.2017.11.015

[16] D. Xu, J. Yu, J. Shen, N. Li, Y. Song, X. Yang, Aerodynamic design optimization of centrifugal compressor blade using parameterized free-form deformation, in: ASME Turbo Expo 2024: Turbomachinery Technical Conference and Exposition, American Society of Mechanical Engineers, 2024, pp. V12DT35A013. https://doi.org/10.1115/GT2024-125778

[17] A. John, N. Qin, S. Shahpar, The influence of parameterisation setup on the constrained adjoint optimisation of transonic fan blades, in: ASME Turbo Expo 2020: Turbomachinery Technical Conference and Exposition, American Society of Mechanical Engineers, 2021, pp. V02DT38A020. https://doi.org/10.1115/GT2020-15352

[18] Z. Tao, W. Li, Z. Guo, Y. Chen, L. Song, J. Li, Aerothermal optimization of a turbine rotor tip configuration based on free-form deformation approach, Int. J. Heat Fluid Flow 110 (2024) 109644. https://doi.org/10.1016/j.ijheatfluidflow.2024.109644

[19] P. Beard, A. Smith, T. Povey, Experimental and computational fluid dynamics investigation of the efficiency of an unshrouded transonic high pressure turbine, Proc. Inst. Mech. Eng. A: J. Power Energy 225 (2011) 1166–1179. https://doi.org/10.1177/0957650911407979

[20] Zeiss, GOM Software is now ZEISS INSPECT, 2023, https://www.zeiss.com/metrology/en/software/metrology-software.html.

[21] P. Virtanen, et al., SciPy 1.0: fundamental algorithms for scientific computing in Python, Nat. Methods 17 (3) (2020) 261–272. https://doi.org/10.1038/s41592-019-0686-2

[22] M. Tezzele, N. Demo, A. Mola, G. Rozza, PyGeM: Python geometrical morphing, Softw. Impacts 7 (2021) 100047. https://doi.org/10.1016/j.simpa.2020.100047

[23] T. Bell, B. Li, S. Zhang, Structured light techniques and applications, in: J.G. Webster (Ed.), Wiley Encyclopedia of Electrical and Electronics Engineering, Wiley, 1st edition, 2016, pp. 1–24. https://doi.org/10.1002/047134608X.W8298

[24] C. Bernal, B. De Agustina, M.M. Marín, A.M. Camacho, Performance evaluation of optical scanner based on blue LED structured light, Procedia Eng. 63 (2013) 591–598. https://doi.org/10.1016/j.proeng.2013.08.261

[25] D.A. Masters, N.J. Taylor, T.C.S. Rendall, C.B. Allen, D.J. Poole, Geometric comparison of aerofoil shape parameterization methods, AIAA J. 55 (5) (2017) 1575–1589. https://doi.org/10.2514/1.J054943

[26] V. Sripawadkul, M. Padulo, M. Guenov, A comparison of airfoil shape parameterization techniques for early design optimization, in: 13th AIAA/ISSMO Multidisciplinary Analysis Optimization Conference, 2010. https://doi.org/10.2514/6.2010-9050

[27] R. Agromayor, N. Anand, M. Pini, L.O. Nord, Multirow adjoint-based optimization of NICFD turbomachinery using a computer-aided design-based parametrization, J. Eng. Gas Turbines Power 144 (41008) (2022). https://doi.org/10.1115/1.4052881

[28] S. Shahpar, L. Lapworth, PADRAM: parametric design and rapid meshing system for turbomachinery optimisation, in: ASME Turbo Expo 2003, Collocated with the 2003 International Joint Power Generation Conference, American Society of Mechanical Engineers Digital Collection, 2009, pp. 579–590. https://doi.org/10.1115/GT2003-38698

[29] S. Shahpar, Analysis of modern fan manufacturing variations and their links to jet-engine performance, Aeronaut. J. 128 (1320) (2024) 273–291. https://doi.org/10.1017/aer.2023.75

[30] D. Kraft, A Software Package for Sequential Quadratic Programming, Deutsche Forschungs- und Versuchsanstalt für Luft- und Raumfahrt Köln: Forschungsbericht, Wiss. Berichtswesen d. DFVLR, 1988.

[31] B.O. Community, Blender - A 3D Modelling and Rendering Package, Blender Foundation, Blender Institute, Amsterdam, 2018. http://www.blender.org.

[32] A. Demargne, R. Evans, P. Tiller, W.N. Dawes, Practical and reliable mesh generation for complex, real-world geometries, in: 52nd Aerospace Sciences Meeting, 2014. https://doi.org/10.2514/6.2014-0119

[33] L. Lapworth, HYDRA-CFD: a framework for collaborative CFD development, in: International Conference on Scientific & Engineering Computation (IC-SEC), Singapore, 2004.

[34] F.R. Menter, Improved Two-Equations k-ω Models for Aerodynamic Flows, Technical Report NASA TM-103975, NASA, 1992.

[35] M. Carta, S. Shahpar, T. Ghisu, Analysis of the aerothermal performance of modern commercial high-pressure turbine rotors using different levels of fidelity, Proc. Inst. Mech. Eng. A: J. Power Energy 238 (8) (2024) 1426 - 1442. https://doi.org/10.1177/09576509241283129

[36] B. Bai, Z. Li, K. Zhang, J. Li, S. Mao, W.F. Ng, Effects of hole blockage on endwall film cooling and vane phantom cooling performances of a transonic turbine vane, J. Eng. Gas Turbines Power 145 (4) (2022) 041001. https://doi.org/10.1115/1.4056094

[37] E. Ogiriki, Y. Li, T. Nikolaidis, T. Isaiah, S. Gowon, Effect of fouling, thermal barrier coating degradation and film cooling holes blockage on gas turbine engine creep life, Procedia CIRP 38 (2015) 228–233. https://doi.org/10.1016/j.procir.2015.07.017